REPORT

www.the-innovation.org

Boosting the oxygen reduction activity on metal surfaces by fine-tuning interfacial water with midinfrared stimulation

Qilin Zhang,[1,11] Yu Wu,[2,11] Hao Sun,[3,11] Zhongjie Zhu,[4] Hongwei Zhao,[2,4] Jinrong Yang,[5,*] Jie Wang,[4] Min Chen,[4] Sanzhao Song,[6] Shiyou Zheng,[3] Dengsong Zhang,[7] Hui Yang,[8,*] Zhi Zhu,[9,*] and Chunlei Wang[10,*]

*Correspondence: jryang@chem.ecnu.edu.cn (J.Y.); yangh_23@sumhs.edu.cn (H.Y.); zhuzhi@usst.edu.cn (Z.Z.); wangchunlei1982@shu.edu.cn (C.W.)

Received: May 15, 2024; Accepted: December 5, 2024; Published Online: January 6, 2025; https://doi.org/10.1016/j.xinn.2024.100754

GRAPHICAL ABSTRACT

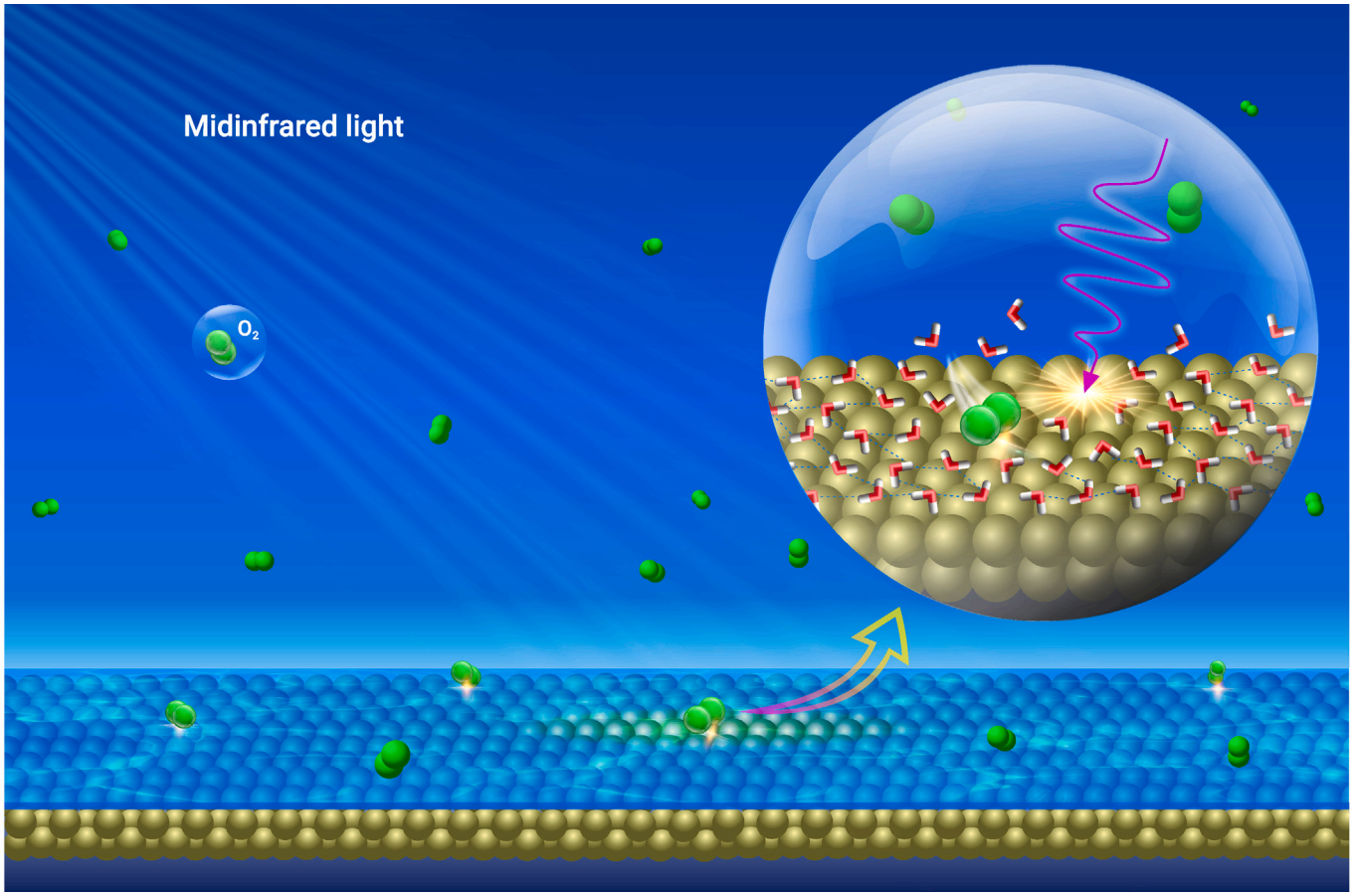

PUBLIC SUMMARY

- Interfacial water on the metal surface acts as a physical barrier preventing efficient catalytic performance.
- The MIRS technique is a novel method for fine-tuning interfacial water structures.
- The application of an appropriate MIRS results in a 50-fold increase in the oxygen reduction activity.
- MIRS can provide a new approach for promoting catalysis and energy conversion and development of photodoped nanofluidic devices.

OPEN ACCESS

REPORT

The Innovation

Boosting the oxygen reduction activity on metal surfaces by fine-tuning interfacial water with midinfrared stimulation

Qilin Zhang,[1,11] Yu Wu,[2,11] Hao Sun,[3,11] Zhongjie Zhu,[4] Hongwei Zhao,[2,4] Jinrong Yang,[5,*] Jie Wang,[4] Min Chen,[4] Sanzhao Song,[6] Shiyou Zheng,[3] Dengsong Zhang,[7] Hui Yang,[8,*] Zhi Zhu,[9,*] and Chunlei Wang[10,*]

[1]School of Mathematics Physics and Finance, Anhui Polytechnic University, Wuhu 241000, China
[2]Shanghai Institute of Applied Physics, Chinese Academy of Sciences, Shanghai 201800, China
[3]School of Materials and Chemistry, University of Shanghai for Science and Technology, Shanghai 200093, China
[4]Shanghai Advanced Research Institute, Chinese Academy of Sciences, Shanghai 201210, China
[5]School of Chemistry and Molecular Engineering, East China Normal University, Shanghai 200062, China
[6]Wenzhou Institute, University of Chinese Academy of Sciences, Wenzhou, Zhejiang 325001, China
[7]Innovation Institute of Carbon Neutrality, Shanghai University, Shanghai 200444, China
[8]College of Medical Instrumentation, Shanghai University of Medicine and Health Sciences, Shanghai 201318, China
[9]School of Optical-Electrical and Computer Engineering, University of Shanghai for Science and Technology, Shanghai 200093, China
[10]International Joint Laboratory of Catalytic Chemistry, College of Sciences, Shanghai University, Shanghai 200444, China
[11]These authors contributed equally
*Correspondence: jryang@chem.ecnu.edu.cn (J.Y.); yangh_23@sumhs.edu.cn (H.Y.); zhuzhi@usst.edu.cn (Z.Z.); wangchunlei1982@shu.edu.cn (C.W.)

Received: May 15, 2024; Accepted: December 5, 2024; Published Online: January 6, 2025; https://doi.org/10.1016/j.xinn.2024.100754

Citation: Zhang Q., Wu Y., Sun H., et al., (2025). Boosting the oxygen reduction activity on metal surfaces by fine-tuning interfacial water with midinfrared stimulation. The Innovation **6(1)**, 100754.

Heterogeneous catalysis at the metal surface generally involves the transport of molecules through the interfacial water layer to access the surface, which is a rate-determining step at the nanoscale. In this study, taking the oxygen reduction reaction on a metal electrode in aqueous solution as an example, using accurate molecular dynamic simulations, we propose a novel long-range regulation strategy in which midinfrared stimulation (MIRS) with a frequency of approximately 1,000 cm^{-1} is applied to nonthermally induce the structural transition of interfacial water from an ordered to disordered state, facilitating the access of oxygen molecules to metal surfaces at room temperature and increasing the oxygen reduction activity 50-fold. Impressively, the theoretical prediction is confirmed by the experimental observation of a significant discharge voltage increase in zinc-air batteries under MIRS. This MIRS approach can be seamlessly integrated into existing strategies, offering a new approach for accelerating heterogeneous reactions and gas sensing within the interfacial water system.

INTRODUCTION

Chemisorption processes on metal surfaces in aqueous solutions generally involve the transport of molecules at the nanoscale, which is the basis of heterogeneous catalysis.[1–3] In interface chemistry, diffusion along surfaces and interfaces is an elementary and often rate-determining step.[4–6] The microscopic kinetics of a reaction in heterogeneous catalysis are usually governed by the transport of the reacting species on the surfaces of the catalysts and thus the speed at which these species reach specific sites where the catalytic reaction occurs. Interfacial water consisting of networks held together by strong hydrogen bonds on the metal surface creates a physical barrier for this diffusion process that hinders the access of the reactant molecules to the active site of the metal surface.[7–9] For example, using molecular dynamics (MD) simulations, a recent study by Wang et al. revealed that the activity of the oxygen reduction reaction (ORR) is different on regular and irregular surfaces in aqueous solutions because of the different adsorption structures of monolayer water (MW).[10] Wang et al. found an enhanced hydrogen evolution reaction on the Pd crystal arising from the MW layer on the Pd surface using electrochemical, *in situ* Raman spectroscopy, and computational techniques.[11] Therefore, manipulation of interfacial MW structures plays a key role in the development of strategies for overcoming the diffusion barrier faced by gaseous molecules, changing material properties, and underpinning schemes to accelerate chemical reactions on metal surfaces.

In the past few decades, numerous strategies have been proposed for tuning the reorientation of water molecules to improve the reaction rate and regulate surface physical properties through interfacial engineering,[12–19] solvent modification,[20–23] and light control,[24–27] but the precise regulation of the interfacial water structure is still at a comparatively early stage of development. For example, while transition metal mixing can tune the surface electronic state and thus tailor the interfacial water structure to enhance the catalytic activity,[28,29] design of alloy nanocrystals with homogeneous configurations is challenging. Enhanced reaction reactivity of interface water can be achieved through a change in the solvent environment,[30,31] which significantly affects the reaction conditions. Recently, Ahn et al. have shown that coherent light-matter states can control chemical reactions based on the strong interactions between molecular vibrations and electromagnetic fields.[32] Compared with the other catalytic processes, photocatalysis is highly advantageous because it provides precise long-range spatiotemporal control.[33,34] Even more encouraging is the emergence of a large number of theoretical and experimental studies on the regulation of thermal effects, phase transitions, structural dissociation, or transport characteristics of water and biological macromolecules by MIRS in recent years.[35–45] Therefore, the development of an appropriate light-based technique for precise regulation of the structure and dynamic properties of interfacial water is vital for improving the photocatalytic performance of metal surfaces.

Taking the sluggish kinetics of the ORR associated with fuel cells as an example,[46] accurate MD simulations demonstrate that the application of midinfrared stimulation (MIRS) with a frequency of approximately 1,000 cm^{-1} can nonthermally increase the rate of O_2 diffusion and access to the metal surface in aqueous solution at room temperature, resulting in an increase of up to ~50 times compared with that in the absence of stimulation. Remarkably, our experimental results confirm the theoretical prediction, verifying the hypothesis that ~1,000 cm^{-1} MIRS can enhance the ORR performance at the metal-water interface. Based on the comparison of the collective vibration spectra (CVS) of bulk water (BW) and MW, this nonthermal effect is attributed to the fact that BW hardly absorbs the MIR electromagnetic radiation at 1,000 cm^{-1}, whereas the MW on the metal surface can strongly absorb the waves at this specific frequency via a resonance mechanism, resulting in the breaking up of the MW H-bond network that repels the O_2 and prevents it from approaching the surface, accordingly promoting the O_2 adsorption rate. These findings are of general significance for understanding the spectral features of interfacial water and increasing the ORR activity of metal surfaces via MIRS.

RESULTS AND DISCUSSION

Regulatory effect of MIRS on the coadsorption of water and O_2 on metal surfaces

Conventionally, the ORR activity of metal catalysts can be improved by increasing the probability of O_2 reaching the surface. However, it is important to note that the presence of a robust and ordered MW network inhibits the adsorption of O_2 on fcc(100) metal surfaces.[9,10,47] Previous reports have clearly revealed that appropriate MIRS can regulate the structure and dynamic properties of water/biomacromolecules via resonance mechanisms.[37–39,41,42,44,45] Here, we investigated the influence of MIRS on the coadsorption of water and oxygen molecules on the fcc(100) metal surface (Pt as an example) via accurate MD simulations with an interface force field (IFF)[48–50] (calculation details in the supplemental information for classical MD simulations), which exhibits extremely high accuracy in simulating the interactions between fcc metals and

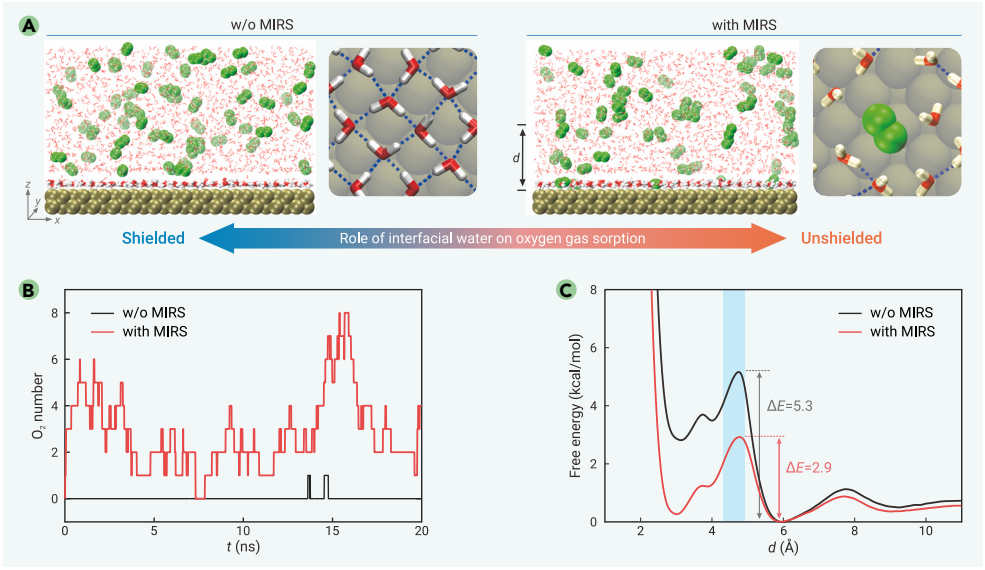

Figure 1. Application of specific MIRS at a frequency of approximately 1,000 cm^{-1} can accelerate the adsorption of O_2 onto metal surfaces, consequently increasing the catalytic reaction rate (A) Snapshots of water (red and white) and O_2 coadsorption on a Pt(100) surface are depicted in side and top views in the presence and absence of MIRS. The Pt atoms, O_2 molecules, and hydrogen bonds (dashed lines) are shown in tan, green, and blue, respectively. (B) Evolution of the number of the O_2 molecules adsorbed on the Pt(100) surface during the simulation time period. The red and black lines correspond to simulations conducted with and without (w/o) MIRS, respectively. (C) Free energy profiles of O_2 near the Pt(100) surface in aqueous solution with (red) and without (black) the external MIRS.

water, particularly with regard to density, surface energy, and interface energy.[49] Interestingly, Figure 1A shows that a considerable amount of O_2 can diffuse to the Pt(100) surface under MIRS with a frequency of 1,000 cm^{-1} (~30 THz) and a strength of 2.0 V/nm. For more details, please see Note S2 and Video S1. The simulations also revealed that, by contrast, O_2 hardly breaks through the MW layer to diffuse onto the Pt(100) surface in the absence of MIRS, which is in accordance with previous studies.[10] For clarity, the side- and top-view sketches of H_2O and O_2 molecule adsorption on Pt(100) are shown in the illustration in Figure 1A. To quantify the activity of O_2, Figure 1B displays the evolution of the number of O_2 molecules adsorbed on the Pt(100) surface during the 20-ns simulation time. The red curve shows a small fluctuation in the number density of O_2 adsorbed on the Pt surface under the MIRS, while the black curve implies that the adsorption of O_2 onto the surface is a low-probability event in the absence of MIRS. According to the results presented in Figure 1B, the average absorption densities are approximately 2.8 ± 0.1 and 0.02 ± 0.01 nm^{-2} in the absence and presence of MIRS, respectively. The sharp contrast between these two values indicates that MIRS is highly effective for the regulation of O_2 diffusion onto Pt(100) electrodes in aqueous solution.

To reveal the mechanism by which MIRS enhances the O_2 adsorption rate, we performed guided MD simulations (see supplemental information for free energy calculations) to estimate the free energy profiles of O_2 near the Pt(100) surface in aqueous solution (as shown in Figure 1C). Without external MIRS, a significant free energy barrier of up to ~5.3 kcal/mol must be overcome for oxygen molecules to diffuse onto the Pt surface; this barrier is considerably larger than the thermal motion energy of O_2 (~1.5 kcal/mol, as evaluated by the equipartition theorem) at room temperature; this explains why it is difficult for O_2 to break through the MW network and then diffuse onto the Pt(100) surface in the absence of MIRS (see Figure 1B). By contrast, under MIRS, the free-energy barrier is notably reduced to ~2.9 kcal/mol, which can be overcome by O_2 with high probability with the aid of thermal fluctuations. These results provide direct evidence that a near-perfectly ordered MW connected by an in-plane hydrogen bonding network can almost completely prevent O_2 from approaching the Pt(100) surface. Fortunately, this protective MW membrane can be disrupted and transformed into a disordered state by the application of an appropriate MIRS, resulting in the loss of its protective function (additional discussion in Note S3). Notably, the Arrhenius law[10] establishes a relationship between the reaction rate k in thermodynamics and the activation energy E_a, i.e., $k \propto e^{-E_a/k_BT}$, where k_B is the Boltzmann constant and T is the temperature. This formula implies that a difference of 2.4 kcal/mol (Figure 1C) in the energy barrier between the system with MIRS and system without MIRS results in a 50-fold increase in the reaction rate. In addition, for the simulations with applied 1,000 cm^{-1} MIRS, the average temperature of the system can be maintained at ~300 K by the Langevin thermostat (Note S4). These findings suggest that appropriate MIRS will be a powerful tool for non-thermal enhancement of the ORR activity of metal catalysts in aqueous solutions.

Experimental verification of the enhanced oxygen adsorption rate on Pt/C electrode surfaces under MIRS

To verify that MIRS can enhance the ORR performance of the water-metal interface, we designed an optical path for the controlled irradiation of MIRS into the air electrode of a zinc-air battery (shown in Figure 2). More experimental details can be found in Note S1.2. We applied a quantum cascade laser (QCL) to generate a frequency-adjustable MIRS coupled with a green guide laser to precisely target the irradiation onto the Pt/C electrode from the left (Figure 2A), where the morphology and elemental mapping analyses of the Pt/C electrode are shown in Figure 2B. During the experiment, the thermal impact of MIRS on the Pt/C electrode was evaluated via Fourier transform infrared spectroscopy. Through monitoring, it was found that the local temperature on the electrode surface changes slightly under MIRS at room temperature (Note S5). As displayed in Figure 2C, a relatively weak absorption at 1,000 cm^{-1} suggests a smaller temperature rise than that of MIRS within the 1,100–1,150 cm^{-1} range. Furthermore, we also observed a discharge voltage difference of 10 mV between the use of the electrolyte with ambient soluble oxygen and that with saturated dissolved oxygen (Figure 2D). Examination of the dependence of the discharge voltage increase on the MIRS frequency under ambient soluble oxygen shows that our results are consistent with the theoretical predictions, indicating an ORR performance enhancement caused by 1,000 cm^{-1} MIRS. Importantly, this enhancement reproduces the impact of increased dissolved oxygen concentration in electrolyte to reach a saturated state (Figures 2D and 2E). Analysis of the discharge voltage increase, laser powerwith varying MIRS frequency and infrared (IR) spectrum shows that despite the lower MIRS power and IR absorbance at 1,000 cm^{-1}, there is a notable increase in the discharge voltage compared with the frequencies in the 1,100–1,150 cm^{-1} range (Figures 2C and 2F). Therefore, MIRS with a specific frequency significantly and nonthermally enhances ORR performance.

Calculation of the CVS of the MW on the Pt(100) surface via MD simulations

The increased adsorption capacity of O_2 onto Pt(100) surfaces in aqueous solution through 1,000-cm^{-1} MIRS regulation is closely related to the unique IR absorption of the MW. Hence, we investigated the IR spectra of interfacial water on an fcc(100) metal model surface, i.e., a Pt(100) surface (Figure 3A). Initially, we performed calculations to determine the density distributions of interfacial water, g(z), as a function of the z coordinate (shown in Figure 3B). The g(z) profile reveals the presence of four distinct regions within interfacial water: the 1st ($0 < z \leq 4$ Å), 2nd ($4 < z \leq 7$ Å), 3rd ($7 < z \leq 25$ Å), and 4th ($z > 25$ Å) regions. Notably, the 1st region has a peak width of ~3 Å, clearly distinguishing the existence of the MW, as observed in Figure 3A. For greater clarity, the top view of the MW forming a quasirhombic H-bond network structure is also shown in the inset of Figure 3B. This MW with a quasi-two-dimensional structure should correspond to a characteristic spectrum in the CVS band. Therefore, we calculated the IR spectrum of the MW via the autocorrelation function (see supplemental information for the calculation of the IR spectrum). For comparison, the BW spectrum is also presented in Figure 3C, where the black (I^{BW}_{total}) and red (I^{MW}_{total}) curves represent the spectral intensities of the MW and BW, respectively. Notably, the CVS band of I^{BW}_{total}, generally

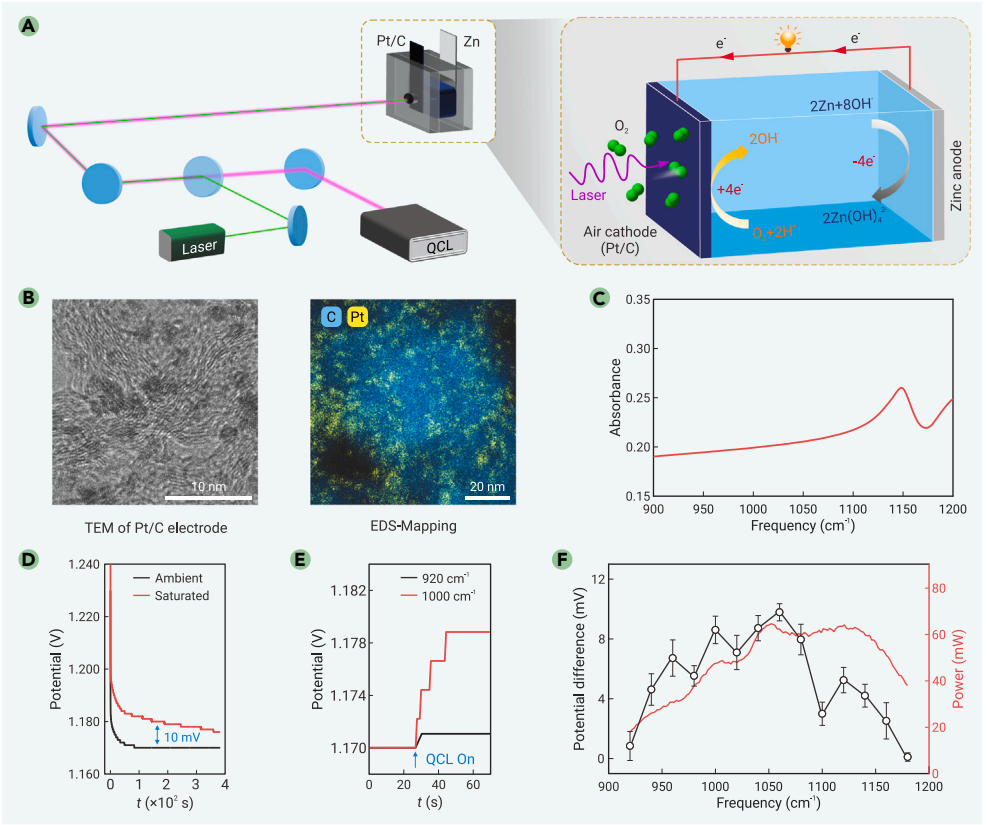

Figure 2. Electrochemical experiments substantiate the proposal that MIRS at a frequency of 1,000 cm^{-1} nonthermally facilitates the ORR process (A) Schematic illustrating the optical path and electrochemical reaction process in the experimental setup, featuring a frequency-adjustable quantum cascade laser (QCL) as the light source and a zinc-air battery as the experimental sample. (B) Morphology and elemental mapping analyses of the Pt/C electrode. (C) Infrared absorption spectroscopy characterization of the Pt/C electrode. (D) Based on the constant current discharge, the discharge voltage of the zinc-air battery is recorded in the instances involving ambient soluble and saturated dissolved oxygen within the electrolyte. (E) MIRS at a specific frequency significantly enhances the discharge voltage of the battery. (F) Enhancements in the discharge voltage induced by MIRS, together with variations in laser power, are observed with the changes in the laser frequency. The error bars were evaluated on the data obtained from three parallel experiments.

reproduces the previous theoretical and experimental results,[51,52] albeit with slight differences attributed to the use of different force field models. In sharp contrast, a clear difference can be observed between the I^{MW}_{total} and I^{BW}_{total} spectral profiles in the CVS band (ω < 1,200 cm^{-1}). Therefore, our subsequent analysis of the spectrum will focus on the CVS band. As displayed in Figure 3C, the CVS band of I^{MW}_{total} is split into a dominant fingerprint peak (F peak) centered at approximately 1,000 cm^{-1} and an accompanying sub-peak (S peak) centered at approximately 600 cm^{-1}. This narrow F peak is clearly far from the half-peak width range (approximately 400–800 cm^{-1}) of the CVS peak of I^{BW}_{total}; this implies that the MW has strong light absorption capacity for 1,000 cm^{-1} MIRS, whereas the corresponding absorption by BW is quite limited. MD simulation revealed significant changes in the average number of H-bonds and the degree of order of the water molecules in the 1st region under 1,000 cm^{-1} MIRS, implying the transition of the MW from an ordered to a disordered structure (Note S6). Notably, additional calculations demonstrate that variations in the electrolyte pH have only a negligible effect on the absorption spectrum of confined water (more discussion in Note S7).

To analyze the CVS feature of the MW, we further decompose the overall spectrum (I^{MW}_{total}) into the normal and horizontal directions (see inset of Figure 3C). Figure 3C shows that the F peak appears only in the I^{MW}_{normal} spectrum but is completely absent in the $I^{MW}_{horizontal}$ spectrum. This result clearly indicates that

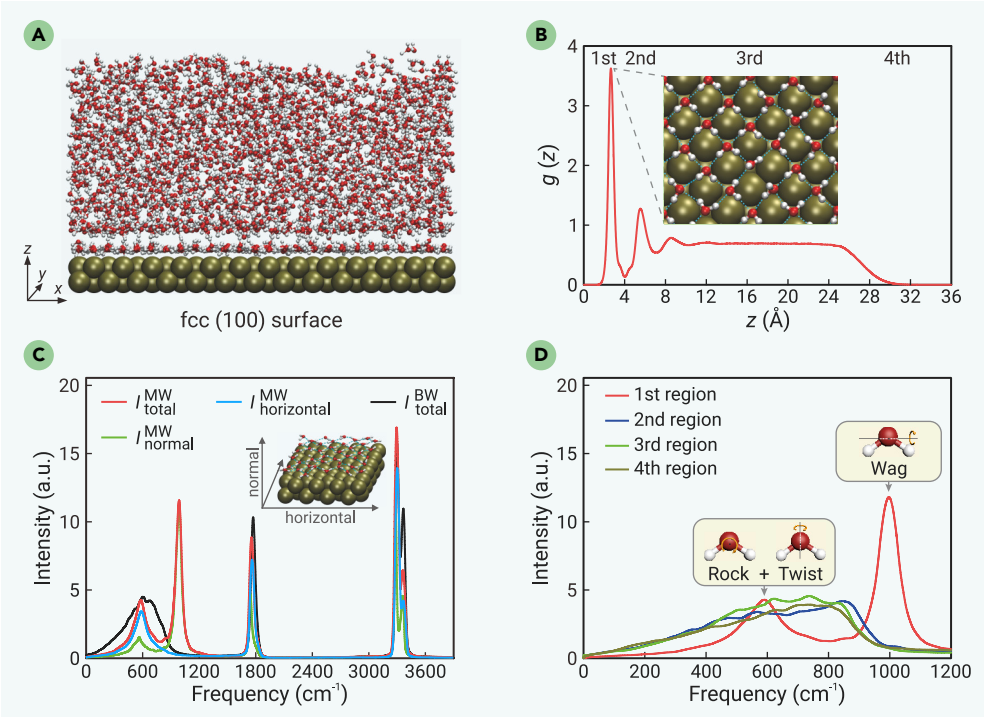

Figure 3. Structural and spectral properties of water on an fcc(100) hydrophilic metal surface (A) Side-view snapshot of a water film with a thickness of approximately 3 nm on a Pt(100) model surface. Tan, red, and white spheres denote platinum, oxygen, and hydrogen atoms, respectively. (B) Water density distributions g(z) as a function of the distance z between the water molecules and the surface along the z direction. (C) IR spectra of bulk water (BW) and monolayer water (MW) on the surface. The black and red curves represent the overall spectra of the BW and the MW, and the green and blue curves represent the spectra of the MW in the normal and horizontal directions (see inset), respectively. (D) IR spectra of interfacial water in the 1st, 2nd, 3rd, and 4th regions below 1,200 cm^{-1}. Insets: sketches of the rock, twist, and wag modes.

Table 1. Frequencies of libration modes for different type of water

Type of water	Binding energy (kcal/mol)	Rock (cm^{-1})	Twist (cm^{-1})	Wag (cm^{-1})
Bulk water	20	520	640	880
Monolayer water	28	610	760	1,040

the F peak is mainly due to the out-of-plane vibration of the MW along the normal direction. Moreover, we also calculate the interfacial water spectrum for the other three regions below 1,200 cm^{-1}. As shown in Figures 3D, a sharp F peak is observed only in the spectrum profile of the MW in the 1st region. These findings provide clear evidence that 1,000 cm^{-1} MIRS can precisely regulate the structural and dynamic properties of MWs on Pt(100) surfaces while avoiding thermal effects in aqueous solutions.

Calculating the frequency of libration modes of water via the harmonic oscillator equation

Next, we sought to identify the vibrational modes corresponding to the F peak and S peak of the MW spectrum. Libration vibrations (including rock, twist, and wag) originate from the hindrance of the rotational motion of water molecules by the restoring force,[53] which is proportional to the binding energy of water molecules. To quantitatively estimate the resonant frequencies for the three librational modes, we employed the harmonic oscillator model equation:[37,54] $E_b = I(2\pi c\omega)^2/2$, where E_b is the average binding energy, I is the moment of inertia of the water molecule along a specific Cartesian axis (see inset of Figure 3D), c is the speed of light, and ω is the vibration frequency. As shown in Table 1, the E_b of the interfacial MW on the model surface is estimated to be ~28 kcal/mol, which is much greater than the value for BW (~20 kcal/mol).[55] Consequently, the wag frequency of the MW is predicted to be approximately 1,040 cm^{-1}, which is close to the F peak center position (~1,000 cm^{-1}) in Figure 3D. Similarly, the frequencies of the rock (610 cm^{-1}) and twist (760 cm^{-1}) librations are also near the position of the S peak. Based on these observations, we inferred that the F peak is due to the wag mode and the S peak is mainly due to the coupling of the rock and twist modes (as shown in the inset of Figure 3D). Due to the robust planar structure of the MW, the out-of-plane vibration of water molecules requires less energy compared with the in-plane vibration, which needs to overcome the strong H-bond binding. As a result, the spectrum intensity of the F peak, dominated by the out-of-plane vibration (wag), is greater than that of the S peak, which corresponds to the suppressed in-plane vibration (rock or twist). More details for the libration modes of water are provided in Note S8.

Estimation of the CVS of the MW using classic MD simulations with polarized-Pt model and first-principles MD simulations

It is important to discuss the influence of the force field on the CVS of MW on Pt(100). Based on the simulation setup in Figure 3A, we modified the nonpolarizable Pt model to a polarizable model with the force field parameters developed by Wang et al.[10] In brief, the Pt atom is transformed to a positive core with a charge of +1e and a dummy electron with a charge of −1e connected by a harmonic spring. A snapshot of the new simulation system with the polarized Pt model is shown in Figure 4A. Using highly accurate MD simulation with the IFF, we re-evaluate the CVS of the MW on the polarized Pt(100) surface. Figure 4B shows that the CVS profiles of MWs for the polarizable and nonpolarizable Pt(100) surfaces are highly consistent. Furthermore, we also performed first-principles MD simulations with the neural network potential developed using the machine learning approach. A snapshot of this simulation is shown in Figure 4C, and more details about the first-principles neural network MD simulations are provided in the supplemental information. In Figure 4C, the density distribution profile of first-layer water shows two adjacent peaks located at 8.2 and 8.9 Å along the normal direction of the Pt surface, which agrees with previous results obtained through quantum mechanics MD.[31] For clarity, the width ranges of the two peaks are defined as R1A and R1B (Figure 4A), respectively, in which the typical structures of water molecules are depicted on the right side of Figure 4B. The left side of Figure 2B shows the CVS of water in R1A (blue) and R1B (red). The CVS of water molecules in R1A presents a sharp peak with a frequency of approximately 946 cm^{-1}. It should be highlighted that, despite the difference in the computed CVS profiles for the Pt surface MW between the first-principles and classical MD simulations, a distinctive F peak at approximately 1,000 cm^{-1} is consistently observed using both methods (more discussion in Note S9). This finding suggests that the manipulation of the properties of interfacial water via an ~1,000 cm^{-1} MIRS without inducing thermal disturbances is feasible.

Investigating the CVS of interfacial water on fcc solid surfaces with different wettabilities

Finally, to generalize the aforementioned findings to other solid materials, a series of simulations were performed by varying the LJ potential parameter of the solid atoms in Figure 3A. Figure 5A shows the density function g(z) of water molecules along the normal direction under different ϵ_r values, where $\epsilon_r = \epsilon/\epsilon_0$ is the ratio of the LJ potential parameters between the solid atom (ϵ) and the Pt atom (ϵ_0). For clarity, the 1st-region curves of g(z) are amplified in Figure 5A (inset), from which we can observe a gradual increase in both the intensity and central frequency of the peaks as ϵ_r increases from 0.01 to 1.0; this implies that the degree of order of the water within the 1st region gradually increases with increasing ϵ_r. To further confirm this observation, the dipole distribution probability of the 1st-region water as a function of average angle $\langle\theta\rangle$ for different ϵ_r values is shown in Figure 5B. As ϵ_r increases from 0.01 to 1.0, the peak height increases while the half-peak width decreases, indicating that $\langle\theta\rangle$ tends to align parallel to the solid interface and that the water structure within the 1st region becomes more ordered. Moreover, we also calculated the CVS of water in the 1st region under different ϵ_r values, as illustrated in Figure 5C. As expected, with increasing ϵ_r, the intensity of the F peak gradually increases and its position gradually blue shifts. These results indicate that a greater hydrophilicity of the solid interface leads to a higher central frequency of the F peak. To further clarify this relationship, Figure 5D displays the order parameters and the central frequencies of the F peak plotted versus ϵ_r. The order parameter values were estimated based on the probability maximum in Figure 5B for different ϵ_r. The three curves exhibit similar increasing trends, all of which increase with increasing ϵ_r. An increase in the potential well parameter values corresponds to an increase in the hydrophilicity of the solid meterial[45,56] (Note S10). Therefore, these results strongly confirm that the center frequency of the F peak blue shifts with increasing interfacial hydrophilicity and degree of order of the interfacial water. For further validation, Figure 5D also shows that the F peak center frequencies obtained from the MD simulation are in good agreement with those calculated theoretically (harmonic oscillator equation) at different ϵ_r values.

CONCLUSION

In summary, combining MD simulations and MIRS experiments, we propose a new strategy to improve the ORR activity of Pt(100) metal surfaces in aqueous solutions at room temperature by applying MIRS with a frequency of approximately 1,000 cm^{-1}. The core mechanism is the excitation of the resonance of MWs on the metal surface via MIRS that disrupts the robust planar water network and reduces the energy barrier of oxygen diffusion to the metal surface. The ORR activity is estimated to increase by ~50 times under MIRS compared with that without MIRS. Importantly, MIRS at this specific frequency can effectively regulate the structure and dynamic properties of MWs on metal surfaces while avoiding thermal effects. Specifically, MD simulations revealed a distinctive fingerprint peak (F peak) of the MW on the metal surface, centered at approximately 1,000 cm^{-1}, which is clearly distinguishable from the CVS of the MW and from the IR absorption band of BW. Thus, MIRS can effectively penetrate BW without being strongly absorbed when regulating MW. Meanwhile, various numerical simulations were used to confirm that the appearance of F peaks is independent of the force field used and that the center frequency of the F peak will blue shift with increasing interaction between the metal surface and MW. Furthermore, we verified through experiments that the application of 1,000 cm^{-1} MIRS can enhance the ORR activity of metal-water interfaces. It is important to note that, beyond the ORR, gas reactions occurring on metal surfaces in aqueous solutions are ubiquitous and include processes such as hydrogen evolution and carbon dioxide reduction. Therefore, our MIRS regulation strategy has the advantages of long-range manipulation, nonthermal effects, and convenient generalization in promoting these reactions on metal surfaces. These findings advance our understanding of fundamental chemical and physical processes at the atomic and molecular levels, contributing to the development of new theories and technologies. They also provide valuable guidance

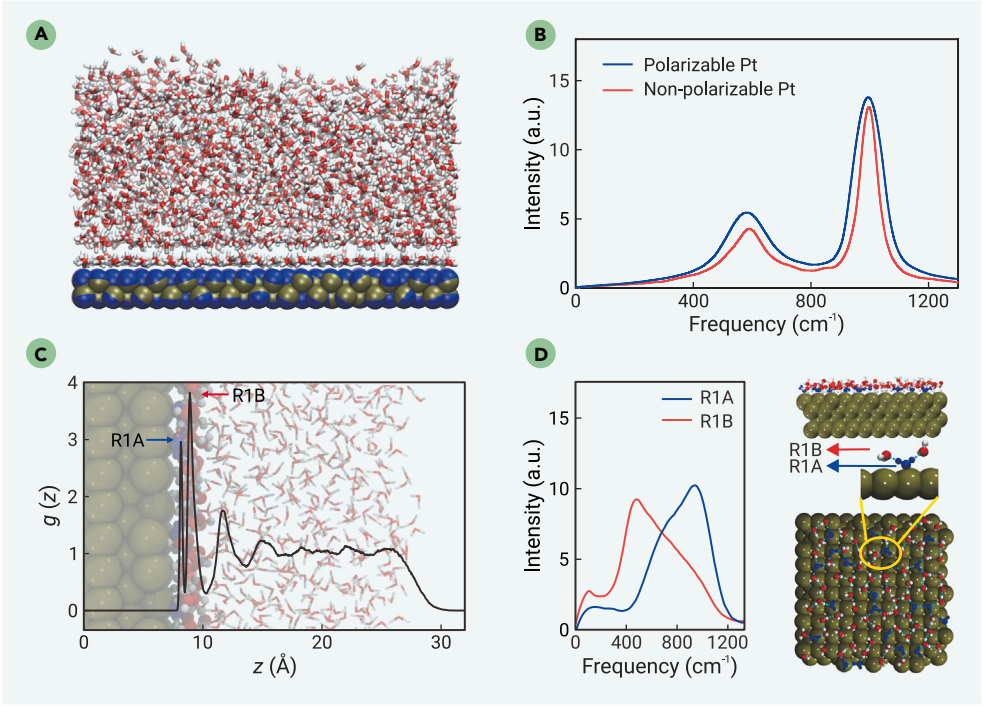

Figure 4. Regardless of the force field used, the interfacial water on the Pt(100) surface shows a CVS spectrum that is different from that of bulk water (A) Side-view snapshot of interfacial water on a polarized-Pt(100) model surface. Tan and blue spheres denote the platinum and pseudo atoms, respectively. (B) Comparison of CVS profiles of the MW on the polarized and nonpolarized Pt(100) surfaces, which are calculated by accurate MD simulations with the IFF. (C) Water density distributions g(z) as a function of the distance z between water molecules and the surface along the z direction. (D) CV spectra of R1A (blue) and R1B (red) calculated by first-principles MD simulations with the neural network potential. Right: typical structures of R1A and R1B on the surface.

for the use of electromagnetic stimulation to enhance catalysis, energy conversion, and gas-sensing processes, as well as in designing new light-driven nanofluid devices.[57,58]

MATERIALS AND METHODS

Classical MD simulations

The classical MD simulations were performed using the NAMD 2.14 package[59] with the CHARMM27 force field[60] in the NVT ensemble at 300 K constant temperature. The flexible TIP3P water model[61] was used in the simulations. The particle-mesh Ewald technique[62] was used to treat long-range electrostatic interactions. A cutoff of 1.2 nm was applied to calculate the electrostatic and Lennard-Jones interactions. Unless otherwise noted, the IIF parameters of the Pt atom[49] were ϵ_0 = 7.8 kcal/mol and σ_0 = 2.535 Å. The fcc(100) solid model was fixed for simplicity in all simulations.

To simulate O_2 diffusion onto the Pt(100) surface, 128 oxygen molecules (ϵ_{OO} = 0.12 kcal/mol and σ_{OO} = 3.029 Å) were randomly dissolved in aqueous solution. A snapshot constructed using the VMD[63] software is shown in Figure 1A. A Pt(100) slab built with the dimensions of 49 × 49 Å^2 along the horizontal direction was soaked in the reservoir with 5,063 water molecules. The three-dimensional simulation box with periodic boundary conditions had the dimensions of 50.96 × 50.96 × 62.0 Å^3 in the x, y, and z directions. Figure S1 shows the periodic structure of the simulation system in the z direction, where a metal sheet is located between the upper and lower water layers, forming a cell (Note S1.1). In these simulations, the time step is 1 fs, the data are recorded every 1 ps, and the total simulation time is 20 ns for each simulation system. The 1,000 cm^{-1} MIRS was uniformly applied to the simulation system along the normal direction of the Pt(100) surface, with specific methods described in previous work.[42] Notably, a high O_2 concentration (~1.4 M) was used in the simulation to obtain good data statistics while avoiding high computational costs.

To calculate the CVS of the MW on Pt(100), a series of systems consisting of fcc(100) solid sheets and water were constructed. Figure 1B shows a representative equilibrium simulation snapshot for a 3-nm-thick water film with 2,740 water molecules on a fcc(100) metal surface with a lattice parameter of 3.92 Å. The solid model was built with the dimensions of 49 × 49 Å^2 dimensions along the horizontal directions. The three-dimensional periodic simulation box had the dimensions of 50.96 × 50.96 × 100 Å^3 in the x, y, and z directions. In this simulation, the time step was set to 0.1 fs, and the data were collected every 10 time steps. The execution time for each simulation was 7 ps, and the last 6 ps of data were used to analyze the IR spectrum of water.

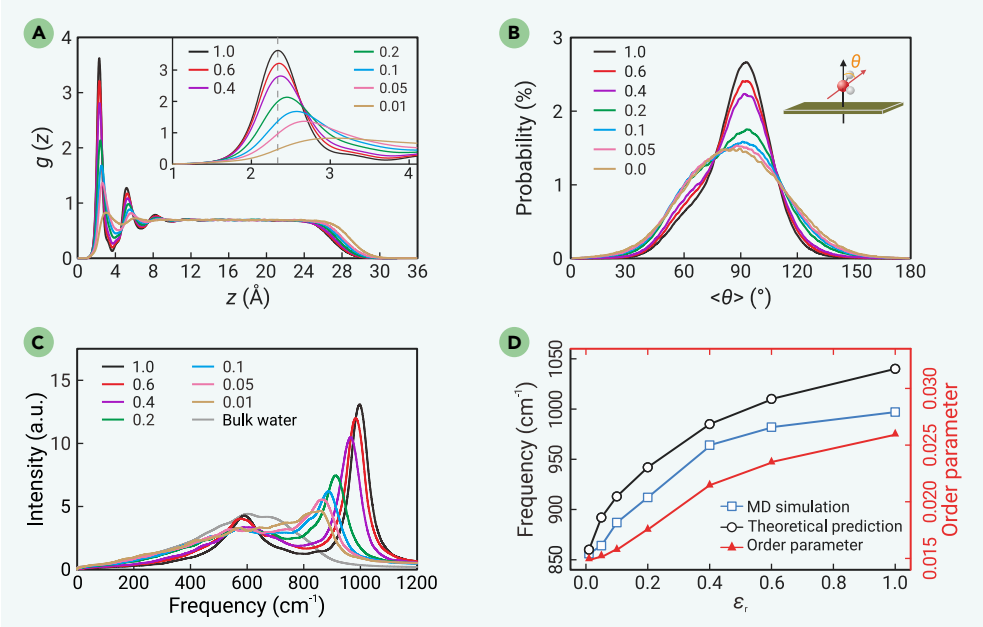

Figure 5. Relationships among the surface potential parameters, degree of order of interfacial water, and F peak location (A) Density profile of water molecules along the normal direction for different ϵ_r values. The first region of the curves is amplified in the inset. (B) Dipole distribution probability of water molecules in the first region as a function of the average angle $\langle\theta\rangle$ for different ϵ_r, where θ represents the dipole-direction angle of the water molecule (see the inset). (C) CVS profiles of water in the 1st region (below ~4 Å) for different ϵ_r values. (D) The order parameters and the position frequencies of the F peak with respect to ϵ_r, where the curves with triangles (black), circles (red), and squares (red) denote the order parameter, theoretically predicted, and MD simulation-derived frequencies, see (C), respectively. The order parameter is estimated based on the probability maximum under different ϵ_r values in (B).

Free energy calculations

The potentials of the mean force (PMF) profiles for O_2 were calculated via collective variable-based calculations with an umbrella sampling algorithm.[64] Steered MD simulations were performed using NAMD in the NVT ensemble at a constant temperature (300 K) maintained by Langevin dynamics. A biased harmonic force with force constants of 2 (lower) and 10 kcal mol^{-1} $Å^{-2}$ (upper) was applied to gradually drag O_2 closer to the Pt(100) surface from 12 to 1.6 Å along the z axis direction in increments of 0.1 Å to obtain a smooth PMF curve profile.

Experimental device fabrication

An optical path was designed to control the irradiation of MIRS into the air electrode of a zinc-air battery. This experimental setup involves the use of a QCL and a green guide laser to generate the frequency-adjustable MIRS and to determine the spot position of the MIRS irradiation, respectively (Figure 2A). During the process, the air electrode serves as a site for the catalytic ORR, where oxygen diffuses into the catalytic layer containing Pt, and the electrochemical reduction reaction occurs at the interface between the catalytic layer and the electrolyte.

Using transmission electron microscopy in conjunction with energy-dispersive X-ray spectroscopy, a comprehensive analysis was conducted to characterize both the morphology and elemental distribution of the Pt/C electrode (shown in Figure 2B). The experimental procedures are described in more detail in Note S1.2.

Calculation of the IR spectrum

The IR spectrum of water is estimated via the Fourier transform of the dipole-moment autocorrelation function as expressed by[65]

$$I(\omega) \propto \int_0^{\infty} \langle M(t) \cdot M(0) \rangle \cos(\omega t) dt, \qquad \text{(Equation 1)}$$

where $I(\omega)$, ω, and t are the spectral density, angular frequency, and time, respectively. $\langle M(t) \cdot M(0) \rangle$ represents the autocorrelation function of the dipole moments of water molecules. $M(t)$ represents the sum of all individual dipole moments of the water molecules at time t.

First-principles neural network MD simulations

First-principles MD simulations based on the ensemble of neutral network potentials provided by Mikkelsen et al.[18,66] are performed using the CP2K software package.[67] The system contains 562 water molecules above the metal Pt(100), where the interface model is composed of p(10 × 10) supercell slabs with four atomic layers. The upper two layers are relaxed, and the lower two layers are fixed. The simulation box has the dimensions of 27.746 × 27.746 × 50 $Å^3$. A CSVR thermostat[68] is used to maintain the system temperature at 300 K within the NVT ensemble, and the time step is set as 0.5 fs.

REFERENCES

1. Henβ, A.K., Sakong, S., Messer, P., et al. (2019). Density fluctuations as door-opener for diffusion on crowded surfaces. Science ***363***: 715–718. https://doi.org/10.1126/science.aav4143.
2. Seh, Z.W., Kibsgaard, J., Dickens, C.F., et al. (2017). Combining theory and experiment in electrocatalysis: Insights into materials design. Science ***355***: eaad4998. https://doi.org/10.1126/science.aad4998.
3. Nonoyama, N., Okazaki, S., Weber, A.Z., et al. (2011). Analysis of oxygen-transport diffusion resistance in proton-exchange- membrane fuel cells. J. Electrochem. Soc. ***158***: B416. https://doi.org/10.1149/1.3546038.
4. Zambelli, T., Barth, J.V., Wintterlin, J., et al. (1997). Complex pathways in dissociative adsorption of oxygen on platinum. Nature ***390***: 495–497. https://doi.org/10.1038/37329.
5. Inaba, M., Jensen, A.W., Sievers, G.W., et al. (2018). Benchmarking high surface area electrocatalysts in a gas diffusion electrode: measurement of oxygen reduction activities under realistic conditions. Energy Environ. Sci. ***11***: 988–994. https://doi.org/10.1039/C8EE00019K.
6. Janik, M.J., Taylor, C.D., and Neurock, M. (2009). First-principles analysis of the initial electroreduction steps of oxygen over Pt(111). J. Electrochem. Soc. ***156***: B126. https://doi.org/10.1149/1.3008005.
7. Allan, M.G., McKee, M.J., Marken, F., et al. (2021). Solvent-controlled O2 diffusion enables air-tolerant solar hydrogen Generation. Energy Environ. Sci. ***14***: 5523–5529. https://doi.org/10.1039/D1EE01822A.
8. Fang, W., Wang, C., Liu, Z., et al. (2022). Physical mixing of a catalyst and a hydrophobic polymer promotes CO hydrogenation through dehydration. Science ***377***: 406–410. https://doi.org/10.1126/science.abo0356.
9. Liu, E., Jiao, L., Li, J., et al. (2020). Interfacial water shuffling the intermediates of hydrogen oxidation and evolution reactions in aqueous media. Energy Environ. Sci. ***13***: 3064–3074. https://doi.org/10.1039/D0EE01754J.
10. Wang, S., Zhu, E., Huang, Y., et al. (2021). Direct correlation of oxygen adsorption on platinum-electrolyte interfaces with the activity in the oxygen reduction reaction. Sci. Adv. ***7***: eabb1435. https://doi.org/10.1126/sciadv.abb1435.
11. Wang, Y.H., Zheng, S., Yang, W.M., et al. (2021). In situ Raman spectroscopy reveals the structure and dissociation of interfacial water. Nature ***600***: 81–85. https://doi.org/10.1038/s41586-021-04068-z.
12. Gao, R., Wang, J., Huang, Z.F., et al. (2021). Pt/Fe2O3 with Pt-Fe pair sites as a catalyst for oxygen reduction with ultralow Pt loading. Nat. Energy ***6***: 614–623. https://doi.org/10.1038/s41560-021-00826-5.
13. Zhang, L., Roling, L.T., Wang, X., et al. (2015). Platinum-based nanocages with subnanometer-thick walls and well-defined, controllable facets. Science ***349***: 412–416. https://doi.org/10.1126/science.aab0801.
14. Lim, B., Jiang, M., Camargo, P.H.C., et al. (2009). Pd-Pt bimetallic nanodendrites with high activity for oxygen reduction. Science ***324***: 1302–1305. https://doi.org/10.1126/science.1170377.
15. Liu, K., Wang, C., Ma, J., et al. (2016). Janus effect of antifreeze proteins on ice nucleation. Proc. Natl. Acad. Sci. USA ***113***: 14739–14744. https://doi.org/10.1073/pnas.1614379114.
16. Guo, P., Tu, Y., Yang, J., et al. (2015). Water-cooh composite structure with enhanced hydrophobicity formed by water molecules embedded into carboxyl-terminated self-assembled monolayers. Phys. Rev. Lett. ***115***: 186101. https://doi.org/10.1103/PhysRevLett.115.186101.
17. Wang, C., Lu, H., Wang, Z., et al. (2009). Stable liquid water droplet on a water monolayer formed at room temperature on ionic model substrates. Phys. Rev. Lett. ***103***: 137801. https://doi.org/10.1103/PhysRevLett.103.137801.
18. Qu, M., Huang, G., Liu, X., et al. (2022). Room temperature bilayer water structures on a rutile TiO2 (110) surface: hydrophobic or hydrophilic? Chem. Sci. ***13***: 10546–10554. https://doi.org/10.1039/D2SC02047E.
19. Zhou, L., and Wang, C. (2024). Diverse phases of water molecules confined at nanoscale. Innov. Mater. ***2***: 100049. https://doi.org/10.59717/j.xinn-mater.2024.100049.
20. Govindarajan, N., Xu, A., and Chan, K. (2022). How pH affects electrochemical processes. Science ***375***: 379–380. https://doi.org/10.1126/science.abj2421.
21. Wang, T., Zhang, Y., Huang, B., et al. (2021). Enhancing oxygen reduction electrocatalysis by tuning interfacial hydrogen bonds. Nat. Catal. ***4***: 753–762. https://doi.org/10.1038/s41929-021-00668-0.
22. Cai, C., Liu, K., Zhang, L., et al. (2023). Atomically local electric field induced interface water reorientation for alkaline hydrogen evolution reaction. Angew. Chem. Int. Ed. ***62***: e202300873. https://doi.org/10.1002/anie.202300873.
23. Sun, Q., Oliveira, N.J., Kwon, S., et al. (2023). Understanding hydrogen electrocatalysis by probing the hydrogen-bond network of water at the electrified Pt-solution interface. Nat. Energy ***8***: 859–869. https://doi.org/10.1038/s41560-023-01302-y.
24. Sakamoto, H., Ohara, T., Yasumoto, N., et al. (2015). Hot-electron-induced highly efficient O_2 activation by Pt nanoparticles supported on Ta_2O_5 driven by visible light. J. Am. Chem. Soc. ***137***: 9324–9332. https://doi.org/10.1021/jacs.5b04062.
25. Hirakawa, H., Hashimoto, M., Shiraishi, Y., et al. (2017). Photocatalytic conversion of nitrogen to ammonia with water on surface oxygen vacancies of titanium dioxide. J. Am. Chem. Soc. ***139***: 10929–10936. https://doi.org/10.1021/jacs.7b06634.
26. Jiao, F., Chen, C., Liu, T., et al. (2024). Insights of water-to-hydrogen conversion from thermodynamics. Innov. Energy ***1***: 100004. https://doi.org/10.59717/j.xinn-energy.2024.100004.
27. Liu, H., Jia, S., Wu, L., et al. (2024). Active hydrogen-controlled CO2/N2/NOx electroreduction: From mechanism understanding to catalyst design. Innov. Mater. ***2***: 100058. https://doi.org/10.59717/j.xinn-mater.2024.100058.
28. Sun, K., Wu, X., Zhuang, Z., et al. (2022). Interfacial water engineering boosts neutral water reduction. Nat. Commun. ***13***: 6260. https://doi.org/10.1038/s41467-022-33984-5.
29. Shen, L.F., Lu, B.A., Li, Y.Y., et al. (2020). Interfacial structure of water as a new descriptor of the hydrogen evolution reaction. Angew. Chem. Int. Ed. ***59***: 22397–22402. https://doi.org/10.1002/anie.202007567.
30. Thorarinsdottir, A.E., Erdosy, D.P., Costentin, C., et al. (2023). Enhanced activity for the oxygen reduction reaction in microporous water. Nat. Catal. ***6***: 425–434. https://doi.org/10.1038/s41929-023-00958-9.
31. Cheng, T., Wang, L., Merinov, B.V., et al. (2018). Explanation of dramatic pH-dependence of hydrogen binding on noble metal electrode: Greatly weakened water adsorption at high pH. J. Am. Chem. Soc. ***140***: 7787–7790. https://doi.org/10.1021/jacs.8b04006.
32. Ahn, W., Triana, J.F., Recabal, F., et al. (2023). Modification of ground-state chemical reactivity via light-matter coherence in infrared cavities. Science ***380***: 1165–1168. https://doi.org/10.1126/science.ade7147.
33. Xu, Y., Kraft, M., and Xu, R. (2016). Metal-free carbonaceous electrocatalysts and photocatalysts for water splitting. Chem. Soc. Rev. ***45***: 3039–3052. https://doi.org/10.1039/C5CS00729A.
34. Guo, Y., Tong, X., and Yang, N. (2023). Photocatalytic and electrocatalytic generation of hydrogen peroxide: principles, catalyst design and performance. Nano-Micro Lett. ***15***: 77. https://doi.org/10.1007/s40820-023-01052-2.
35. Li, Y., Zhu, Z., Sun, L., et al. (2022). Physicochemical insights on terahertz wave diminished side effects of drugs from slow dissociation. ACS Nano ***16***: 8419–8426. https://doi.org/10.1021/acsnano.2c02952.
36. Zhang, C., Yuan, Y., Wu, K., et al. (2022). Driving DNA origami assembly with a terahertz wave. Nano Lett. ***22***: 468–475. https://doi.org/10.1021/acs.nanolett.1c04369.
37. Zhang, Q.L., Yang, R.Y., Jiang, W.Z., et al. (2016). Fast water channeling across carbon nanotubes in far infrared terahertz electric fields. Nanoscale ***8***: 1886–1891. https://doi.org/10.1039/C5NR07281F.

38. Zhu, Z., Chen, C., Chang, C., et al. (2021). Terahertz-light induced structural transition and superpermeation of confined monolayer water. ACS Photonics ***8***: 781–786. https://doi.org/10.1021/acsphotonics.0c01336.
39. Sun, T., and Zhu, Z. (2022). Light resonantly enhances the permeability of functionalized membranes. J. Membr. Sci. ***662***: 121026. https://doi.org/10.1016/j.memsci.2022.121026.
40. Peng, W., Zhu, Z., Lou, J., et al. (2023). High-frequency terahertz waves disrupt Alzheimer's β-amyloid fibril formation. eLight ***3***: 18. https://doi.org/10.1186/s43593-023-00048-0.
41. Tan, Y., Zhao, H., Wang, W.M., et al. (2022). Water based coherent detection of broadband terahertz pulses. Phys. Rev. Lett. ***128***: 093902. https://doi.org/10.1103/PhysRevLett.128.093902.
42. Zhang, Q.L., Yang, R.Y., Wang, C.L., et al. (2022). Ultrafast active water pump driven by terahertz electric fields. Phys. Rev. Fluids ***7***: 114202. https://doi.org/10.1103/PhysRevFluids.7.114202.
43. Yang, R.Y., Huo, P.Y., Zhang, Q.L., et al. (2023). Strong amplification of mid-infrared radiation absorption in nanotube-confined water. Phys. Fluids ***35***: 052003. https://doi.org/10.1063/5.0142331.
44. Zhu, Z., Zhu, J., Chang, C., et al. (2024). Tunable Surface Wettability via Terahertz Electrowave Controlled Vicinal Subnanoscale Water Layer. Nano Lett. ***24***: 3243–3248. https://doi.org/10.1021/acs.nanolett.4c00248.
45. Zhang, Q.L., Zhou, T., Chang, C., et al. (2024). Ultrahigh-flux water nanopumps generated by asymmetric terahertz absorption. Phys. Rev. Lett. ***132***: 184003. https://doi.org/10.1103/PhysRevLett.132.184003.
46. Ma, Z., Cano, Z.P., Yu, A., et al. (2020). Enhancing oxygen reduction activity of Pt-based electrocatalysts: From theoretical mechanisms to practical methods. Angew. Chem. Int. Ed. ***59***: 18334–18348. https://doi.org/10.1002/anie.202003654.
47. Duan, Z., and Wang, G. (2013). Comparison of reaction energetics for oxygen reduction reactions on Pt (100), Pt (111), Pt/Ni (100), and Pt/Ni (111) surfaces: a first-principles study. J. Phys. Chem. C ***117***: 6284–6292. https://doi.org/10.1021/jp400388v.
48. Lu, J., Xue, Y., Bernardino, K., et al. (2021). Enhanced optical asymmetry in supramolecular chiroplasmonic assemblies with long-range order. Science ***371***: 1368–1374. https://doi.org/10.1126/science.abd8576.
49. Heinz, H., Vaia, R.A., Farmer, B.L., et al. (2008). Accurate simulation of surfaces and interfaces of face-centered cubic metals using 12-6 and 9-6 Lennard-Jones potentials. J. Phys. Chem. C ***112***: 17281–17290. https://doi.org/10.1021/jp801931d.
50. Fang, G., Li, W., Shen, X., et al. (2018). Differential Pd-nanocrystal facets demonstrate distinct antibacterial activity against Gram-positive and Gram-negative bacteria. Nat. Commun. ***9***: 129. https://doi.org/10.1038/s41467-017-02502-3.
51. Heyden, M., Sun, J., Funkner, S., et al. (2010). Dissecting the thz spectrum of liquid water from first principles via correlations in time and space. Proc. Natl. Acad. Sci. USA ***107***: 12068–12073. https://doi.org/10.1073/pnas.0914885107.
52. Yu, C.C., Chiang, K.Y., Okuno, M., et al. (2020). Vibrational couplings and energy transfer pathways of water's bending mode. Nat. Commun. ***11***: 5977. https://doi.org/10.1038/s41467-020-19759-w.
53. Lepodise, L.M., Horvat, J., and Lewis, R.A. (2013). Collective librations of water molecules in the crystal lattice of rubidium bromide: experiment and simulation. Phys. Chem. Chem. Phys. ***15***: 20252–20261. https://doi.org/10.1039/C3CP53667J.
54. Zhang, Q.L., Jiang, W.Z., Liu, J., et al. (2013). Water transport through carbon nanotubes with the radial breathing mode. Phys. Rev. Lett. ***110***: 254501. https://doi.org/10.1103/PhysRevLett.110.254501.
55. Hummer, G., Rasaiah, J.C., and Noworyta, J.P. (2001). Water conduction through the hydrophobic channel of a carbon nanotube. Nature ***414***: 188–190. https://doi.org/10.1038/35102535.
56. Xu, Z., Gao, Y., Wang, C., et al. (2015). Nanoscale hydrophilicity on metal surfaces at room temperature: coupling lattice constants and crystal faces. J. Phys. Chem. C ***119***: 20409–20415. https://doi.org/10.1021/acs.jpcc.5b04237.
57. Hou, L., Liu, X., Ge, X., et al. (2023). Designing of anisotropic gradient surfaces for directional liquid transport: Fundamentals, construction, and applications. Innovation ***4***: 100508. https://doi.org/10.1016/j.xinn.2023.100508.
58. Song, Y., Xu, W., Liu, Y., et al. (2022). Achieving ultra-stable and superior electricity generation by integrating transistor- like design with lubricant armor. Innovation ***3***: 100301. https://doi.org/10.1016/j.xinn.2022.100301.
59. Phillips, J.C., Braun, R., Wang, W., et al. (2005). Scalable molecular dynamics with NAMD. J. Comput. Chem. ***26***: 1781–1802. https://doi.org/10.1002/jcc.20289.
60. MacKerell, A.D., Bashford, D., Bellott, M., et al. (1998). All-atom empirical potential for molecular modeling and dynamics studies of proteins. J. Phys. Chem. B ***102***(18): 3586–3616. https://doi.org/10.1021/jp973084f.
61. Alexiadis, A., and Kassinos, S. (2008). Influence of water model and nanotube rigidity on the density of water in carbon nanotubes. Chem. Eng. Sci. ***63***(10): 2793–2797. https://doi.org/10.1016/j.ces.2008.03.004.
62. Darden, T., York, D., and Pedersen, L. (1993). Particle mesh Ewald: An N ·log (N) method for Ewald sums in large systems. J. Chem. Phys. ***98***: 10089–10092. https://doi.org/10.1063/1.464397.
63. Humphrey, W., Dalke, A., and Schulten, K. (1996). VMD: Visual molecular dynamics. J. Mol. Graph. ***14***: 33–38. 27-28. https://doi.org/10.1016/0263-7855(96)00018-5.
64. Fiorin, G., Klein, M.L., and Hénin, J. (2013). Using collective variables to drive molecular dynamics simulations. Mol. Phys. ***111***: 3345–3362. https://doi.org/10.1080/00268976.2013.813594.
65. Praprotnik, M., and Janežič, D. (2005). Molecular dynamics integration and molecular vibrational theory. III. The infrared spectrum of water. J. Chem. Phys. ***122***(17): 174103. https://doi.org/10.1063/1.1884609.
66. Mikkelsen, A.E.G., Schiøtz, J., Vegge, T., et al. (2021). Is the water/Pt(111) interface ordered at room temperature? J. Chem. Phys. ***155***: 224701. https://doi.org/10.1063/5.0077580.
67. Kühne, T.D., Iannuzzi, M., Del Ben, M., et al. (2020). CP2K: An electronic structure and molecular dynamics software package- Quickstep: Efficient and accurate electronic structure calculations. J. Chem. Phys. ***152***: 194103. https://doi.org/10.1063/5.0007045.
68. Bussi, G., Donadio, D., and Parrinello, M. (2007). Canonical sampling through velocity rescaling. J. Chem. Phys. ***126***: 014101. https://doi.org/10.1063/1.2408420.

ACKNOWLEDGMENTS

We gratefully acknowledge Prof. Te Ji for the helpful discussion. The work was supported by the NNSFC (grant nos. 12022508, 12374214, 12074394, T2241002, 22203032, 62075225, and 11604001), Anhui Provincial Natural Science Foundation (2408085MA008), the Key Scientific Research Foundation of the Education Department of Province Anhui (2023AH050907), sponsored by Shanghai Rising-Star Program (23QA1404200), the Program of Shanghai Academic Research Leader (23XD1421400), and Science and Technology Projects of City Wuhu (2023jc08), China. The computing resources are partly provided by the horizontal cooperation project (HX-2024-05-064), Shanghai Snowlake Technology Co. Ltd., and Shanghai Supercomputer Center of China. The experimental conditions are supported by the BL06B infrared station of the Shanghai Synchrotron Radiation Facility.

AUTHOR CONTRIBUTIONS

C.W., Z.Z., J.Y. and Q.Z. conceived the research idea. Q.Z. carried out the classic MD simulations and data analysis. W.Y., H.S., Z.J.Z., H.W. Z., J.W. and Z.Z. performed the MIRS experiments. J.Y. performed the AIMD calculations and analysis. C.W., J.Y., H.Y. and Z.Z. supervised and guided the research. S.Z.S., S.Y. Z, H.Y., and D.S.Z made good suggestions that improve the manuscript. Q.Z., J.Y, Z.Z. and C.W. wrote the paper. C.W. gave final approval to the manuscript submitted. All authors discussed the results of simulations and experiments.

DECLARATION OF INTERESTS

The authors declare no competing interests.

SUPPLEMENTAL INFORMATION

It can be found online at https://doi.org/10.1016/j.xinn.2024.100754.

LEAD CONTACT WEBSITE

https://www.shu.edu.cn/info/1609/345355.htm; https://oece.usst.edu.cn/_s187/2020/0406/c9442a217365/page.psp.